Volumetric additive manufacturing of SiOC by xolography

Abstract

Additive manufacturing (AM) of ceramics has significantly contributed to advancements in ceramic fabrication, solving some of the difficulties of conventional ceramic processing and providing additional possibilities for structure and function of components. However, defects induced by the layer-by-layer approach on which traditional AM techniques are based still constitute a challenge to address. This study presents volumetric AM of a SiOC ceramic from a preceramic polymer using xolography, a linear volumetric AM process that allows to avoid the staircase effect typical of other vat photopolymerization techniques. Besides optimizing the trade-off between preceramic polymer content and transmittance, a pore generator was introduced to create transient channels for gas release before decomposition of the organic constituents and moieties, resulting in crack-free solid ceramic structures even at low ceramic yield. The viscosity of the resin formulation was optimized without compromising transmittance by addition of fumed silica, leading to optimized viscosity of 5.3 Pa·s and transmittance of 52.7 and 32.4 % at 600 and 405 nm, respectively. Meanwhile, formulation optimization alleviated sinking of printed parts during printing and prevented shape distortion. With the optimization of printing parameters, including UV irradiance and moving speed, solid and porous ceramic structures with a smooth surface and sharp features were fabricated. This work provides a new method for the AM of ceramics at μm/mm scale with high surface quality and large geometry variety in an efficient way, opening the possibility for applications in fields such as micromechanical systems, including transmission systems, reducers, automotive engines, bearings, and microelectronic components.

Keywords: volumetric additive manufacturing, ceramics, preceramic polymer, xolography

1. Introduction

Additive manufacturing of ceramic components from preceramic polymers has recently garnered considerable attention due to the favorable processing features of the precursor systems as well as the range of interesting properties of the resulting materials[1-4]. In particular, photocurable systems have enabled the fabrication of parts with complex structure and high resolution, using Digital Light Processing (DLP) and Stereo Lithography Apparatus (SLA)[5-14] or Two Photon Polymerization (TPP)[15-21]. For DLP and SLA, processing involves selective layer-by-layer curing of a liquid photopolymer under irradiation (usually UV light)[22], enabling the fabrication of rather large and sophisticated parts with sub-millimeter details. However, as demands continue to rise for high surface quality and fast fabrication of increasingly intricate and detailed structures, there are still some challenges to address. For instance, in SLA and DLP process, a specific procedure is required for leveling the liquid surface or refilling the printing area between photopolymerizations of successive layers. This typically results in an anisotropy associated to the layers' interfaces and suboptimal surface quality attributed to the stair stepping effect[23, 24]. Although the recently developed continuous liquid interface production (CLIP) technique[25-27] allows for continuous and fast manufacturing, the solid 3D structures are difficult to print because of the slow refilling of the photocurable liquid. In addition, when building parts with overhangs, the adding and removing of support structures during and after printing complicate the processing and may induce damages to the manufactured components. In the case of

TPP, despite a much higher resolution at the sub-micron scale, the components fabricated by this method are typically smaller than 1 mm^3, which is inadequate for macro-scale applications.

Recently, a linear volumetric additive manufacturing (VAM) technique named xolography was developed, enabling the rapid fabrication of objects with complex structural features and high resolution.[28, 29] The technology is based on dual-color photopolymerization and intersecting of light beams of different wavelengths, in which image patterns generated by visible light are projected on the excited printing zone of a sheet of UV light[28, 29]. Owing to the continuous linear and relatively fast movement of the cuvette containing the photocurable resin, the typical limitations of other vat photopolymerization technologies, such as slow speed and geometric constrains (poor surface quality and impossibility of printing enclosed parts), can be overcome. Furthermore, the use of a viscous resin, which is necessary to mitigate undesired displacement of the part during printing, facilitates the fabrication of large overhangs without any support. Differing from other VAM techniques such as computed axial lithography (CAL)[30-37], where selective solidification of the building volume is achieved in a rotating resin container by the superposition of light exposure from multiple angles, and feedback optimization is required for compensating the non-linear response of the resin to light, xolography operates by combining the intersection of orthogonal lights with the linear movement of the build volume. Therefore, there is no need for feedback optimization, and higher resolutions can be achieved (about ten times than CAL).[28, 29] Recently Corrigan et al.[38] developed different applicable resins for polymeric multi-material VAM with xolography to achieve materials with tunable fluorescence. However, this indirect two-step overprinting strategy didn’t release yet the full potential of xolography, as more types

of materials suitable for the technology other than polymers need to be tested and developed. Considering the demand of sophisticated ceramic architectures with fine details and overhanging features for advanced applications, employing xolography for ceramic fabrication using preceramic polymers could provide significant advantages. Although volumetric AM of SiOC ceramic was recently reported by Kollep et al[39] using the CAL technique, crack issues and surface quality of the printed parts are definitely still a challenge.

Here in this work, ceramic components with smooth surface and complex structures were fabricated by xolography for the first time using a preceramic polymer. The cuvette containing the photocurable resin moves in the printing direction (parallel to the visible light projecting the image to be printed), while a fixed UV light sheet shines perpendicularly through the cuvette inducing local polymerization inside a confined monomer volume (**Figure 1a**). Within the irradiated material, a dual-color photo-initiator (DCPI) undergoes a transition from the ground state to an excited state upon exposure to UV irradiation. Subsequently, it absorbs the visible light coming from a projector containing the information relative to the shape to be printed, thereby enabling selective curing at the place where UV and visible light intersect. The continuous movement during printing without pause facilitates the retention of the structural integrity and the creation of a smooth surface without the formation of layer-to-layer interfaces. **Figure 1b** shows a hollow cubic cage with a ball suspended inside that was printed in a cuvette by xolography. With supporting for the ball provided by the surrounding un-polymerized resin, such a separate and suspended structure could be fabricated without the need for supports and the risks associated to their removal, as typical for traditional vat photopolymerization methods. After extraction from the cuvette, cleaning, freeze drying and pyrolysis, the sample maintained the given shape

and a SiOC ceramic part without cracks nor residual pores was obtained.

A commercially available polysiloxane resin (H44) with a high ceramic yield was used as the ceramic source, and mixed with two photocurable resins (diurethane dimethacrylate (UDMA) and poly (ethylene glycol) diacrylate (PEGDA)). UDMA is the main photopolymer, able of fast crosslinking under the activation of produced free radicals and of imparting higher rigidity to the printed part, favoring its later removal from the vat. However, the solubility of H44 in UDMA is low while it is high in PEGDA, and therefore PEGDA was added to increase the content of H44 without decreasing the ability of crosslinking during photopolymerization. Some fumed silica was also added to optimize the viscosity, and camphor acted as a transient pore generator for the release of decomposition gases during pyrolysis. As type II photo-initiator, a proprietary DCPI was employed according to previous literature[28], to enable polymerization with the assistance of 1-dimethylamino-2-propanol as co-initiator. This amine was selected due to its ability to act as a proton donor and its high chain transfer reactivity in polymerization[40]. In addition, the aminyl free radical tends to react with hydrogen to form peroxyradical, which in turn reacts with amine to restart chain propagation[41] (see **Figure S1**). **Figure 1c** illustrates the mechanism of free radical production including excitation under UV and visible light, fast electron transfer and proton abstraction. Notably, it is the amine radical produced from the co-initiator that possesses high reactivity to activate polymerization, whereas the radical from the photo-initiator does not react significantly, due to steric effects and resonance stability[42]. The schematic evolution of the chemical structure of the material is presented in **Figure 1d**, from curing to pyrolysis.

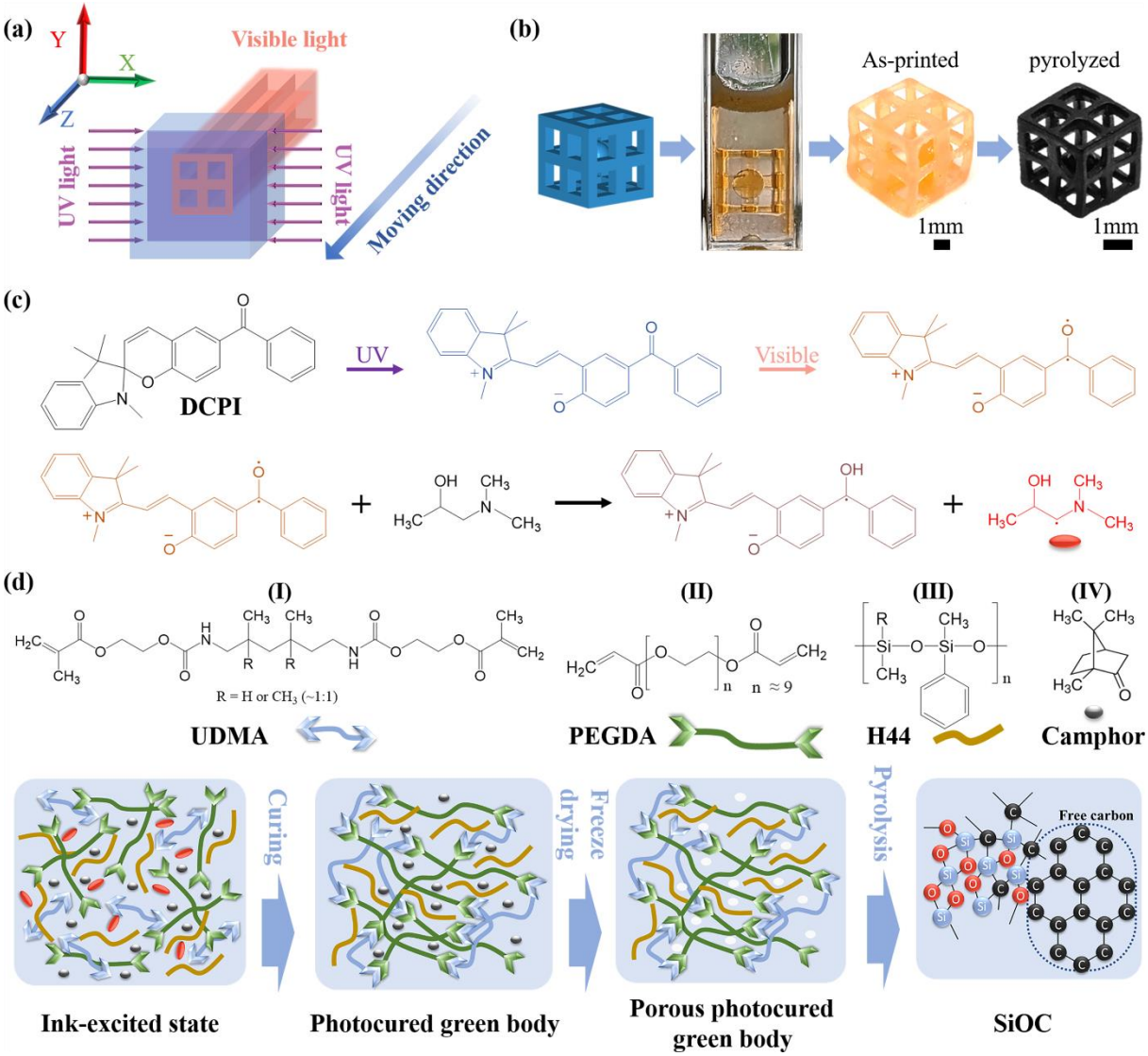

Figure 1. a) Schematic diagram of the printing process: a cuvette is installed on a mobile stage with a UV light sheet passing through in the X-Y plane and moves in the Z direction, while visible light patterns are continuously projected along the Z direction to selectively and locally cure the photopolymer system at the intersection with the UV light sheet. b) 3D model of a ball-in-cage structure and printed sample suspended inside the cuvette, after extraction and pyrolysis. c) Mechanism of radical production: DCPI transfers from the ground state to an excited state under UV light and then absorbs visible light to produce an intermediate, with which the co-initiator reacts to produce aminyl (responsible for initiation) and ketyl radicals. d) Chemical structures and schematics of the feedstock components, as well as the evolution from curing to

pyrolysis.

2. Results and Discussion

2.1. Formulation optimization with respect to transmittance and viscosity

Differing from the printing of a polymer material, which typically requires no heating post-treatment, the aim of this work was to fabricate a ceramic from a preceramic polymer using xolography, achieved through pyrolysis of a printed green body. Therefore, a high ceramic yield of the processed material is required generally to avoid cracking which may occur due to the large gas release and volume shrinkage during pyrolysis. However, to enable xolography, the resin should be as transparent as possible at the working wavelengths (405 and 600 nm for xolography) to avoid the absorption and scattering of light, otherwise the resolution of the printed parts would be severely decreased or the part would not be printed due to insufficient radiation penetration within the cuvette. Consequently, there is a trade-off between obtaining a crack-free ceramic and a high-resolution and printable part as a function of the content of H44. It is difficult to solve this problem by only adjusting the ratio between the photopolymer and H44, especially when a solid structure with ~1-10 mm thickness is desired. In fact, **Figure S2** reports images of the pyrolyzed samples with different content of H44 varying from 33 to 57 wt%, showing both the presence of cracks after pyrolysis and an increased loss of resolution. To solve this challenge, camphor was introduced into the resin formulation to act as generator of transient porosity, facilitating the release of gases from the decomposition of the photopolymers during pyrolysis[43]. It was anticipated that camphor would be eliminated by freeze drying before the heat treatment, and at low temperature during pyrolysis. It is well known that transient, not permanent porosity is generated also during the pyrolysis of a preceramic polymer

component, due to the release of decomposition gases, but at temperatures higher than that of the volatilization of camphor.[44] Thermogravimetric data (**Figure 2a)** indicates that camphor volatilizes in the ~100 to 200°C temperature interval, well ahead of the decomposition of UDMA and PEGDA, occurring in the 200-450°C and 270-430°C range, respectively. **Figure 2b,c** shows SEM images of the samples without and with camphor after freeze-drying and a thermal treatment at 200°C for 1h in nitrogen. It reveals the presence of nanopores in the hundreds of nanometers range, confirming the formation of a network of channels created by the removal of camphor. In contrast with a feedstock without camphor (**Figure S3a**), pyrolyzed samples (shamrock structures (Φ4.3 × 0.8 mm^3 after pyrolysis)) produced from a feedstock containing camphor (**Figure S3b**) possess a crack-free and smooth surface as well as a good resolution, also in the printing direction. No staircase effect is visible perpendicular to the printing direction, which always occurs in traditional layer-by-layer printing technologies, indicating the superiority of this method for producing high quality structures. It's worth noting that no defects like pores or cracks are observed in the cross-section of a fracture (**Figure S3c**), indicating that the pores created from camphor are healed during ceramization at high temperature after the removal of all organic constituents.

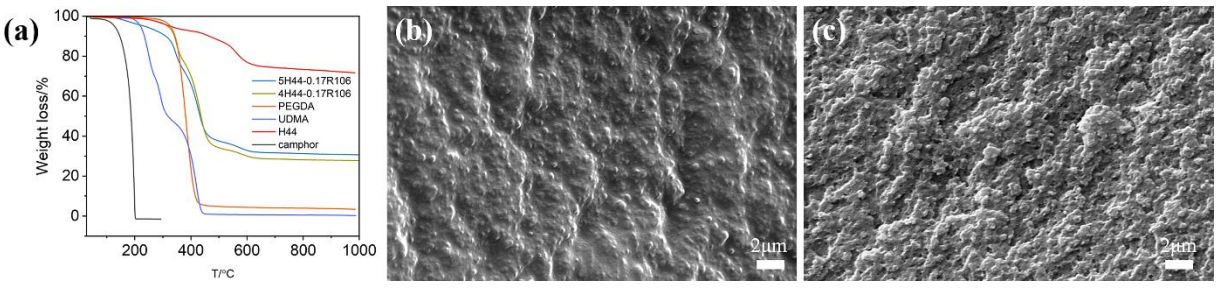

Figure 2. a) TG analysis of two formulations and each individual component: camphor decomposes completely at 200 °C, before UDMA and PEGDA, confirming its function of creating channels for the release of decomposition gases to avoid crack formation.

The two printable formulations had a ceramic yield of 30.6 and 27.7 wt%. b) and c): SEM of the fracture surface of printed samples without and with camphor, freeze-dried and thermally treated at 200°C for 1h.

With the assistance of camphor, it is possible to obtain crack-free ceramics with xolography using a limited amount of H44 to further enhance the resolution. Here, formulations with different amounts of H44 were investigated in terms of their transmittance in the wavelength region of interest. As reported in **Figure 3b**, transmittance at 600 and 405 nm shows a 19 and 28.5% increase, respectively, with a 5% decrease in the H44 content (comparison between formulations with 34.3 (sample 4H44-0.17R106) and 39.5 wt% H44 (sample 5H44-0.17R106)), leading to higher resolution of the printed structures (see **Figure S4**). Indeed, the printed bust of Galileo Galilei produced using the feedstock containing the lower amount of H44 shows finer facial details, such as recognizable eyes and nostrils, although the ceramic conversion occurs with a larger linear shrinkage of 46 % and a small ceramic yield of 27.7 wt%. Notably, the Galileo Galilei statue is a solid structure with a thickness of 3.5 mm (6.5 mm before pyrolysis) and a specific thickness over ceramic yield ratio of 126.4 μm/wt%, which is generally very difficult to obtain without cracks using preceramic polymers[43]. We can therefore conclude that the introduction of camphor not only reduces the preceramic resin content needed to achieve higher resolution, but also helps to produce thicker, bulk ceramic parts free of cracks.

In addition to a suitably high transmittance, an appropriate viscosity in the range of 1-20 Pa·s is also required to enable xolography, especially when building non-supported overhang structures. In fact, a too low viscosity leads to the sinking of the printed part during printing and distorts the suspended features, considering that the

sinking rate is inversely proportional to the viscosity according to Stokes's law.[45] With addition of a very limited amount of fumed silica, viscosity becomes high enough (5.3 and 7.9 Pa·s in this case, respectively) (**see Figure 3c**) to provide efficient support during the whole printing process, with neglectable sinking speed in terms of the printing time (**see Figure 1b and 3c,** green body inside cuvette). Although xolography of photocurable systems with higher viscosity can also be carried out, the extraction from the cuvette and cleaning of the printed part might then become challenging. Moreover, a high viscosity hinders the diffusion of reactive species reducing the polymerization speed.

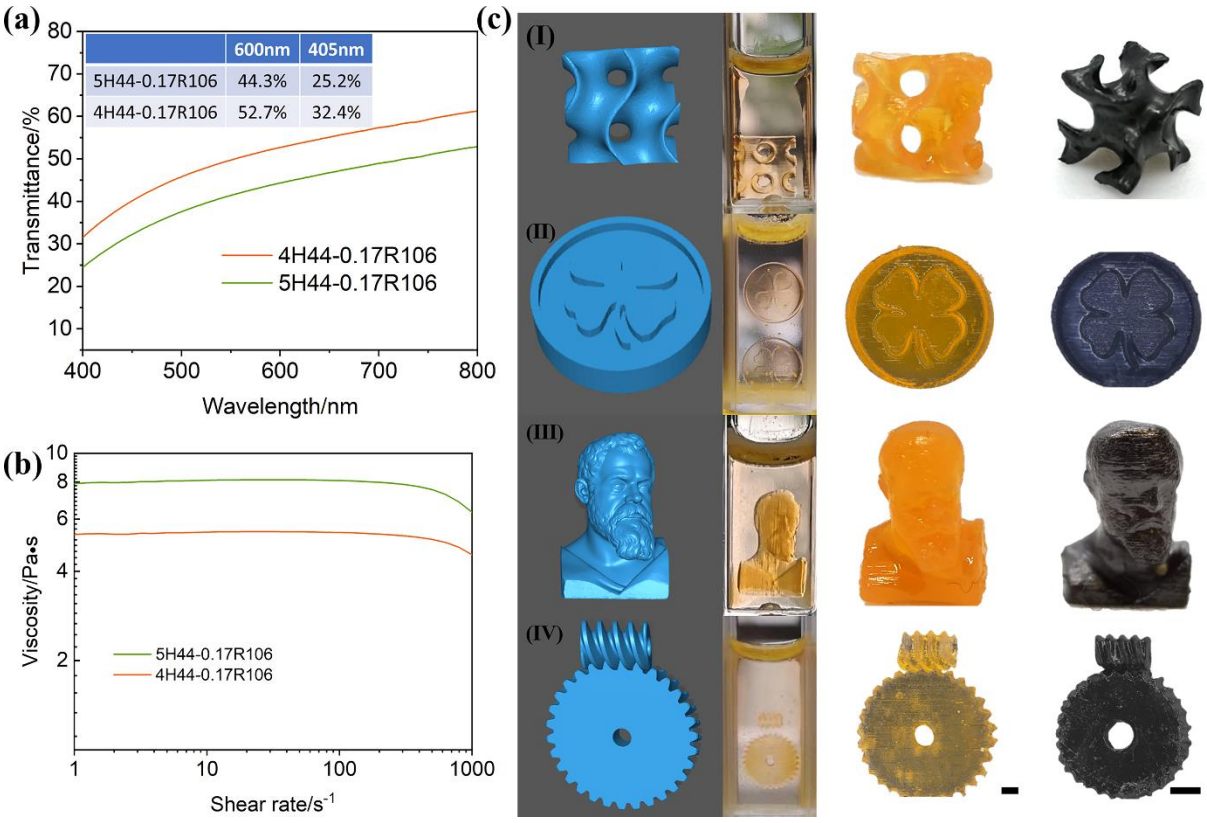

Figure 3. a) Transmittance tests show that lower H44 content helps to increase transmittance at 600 and 405 nm from 44.3 and 25.2 to 52.7 and 32.4 %, respectively. b) Flow curve: viscosity of the two formulations was 5.62 and 7.9 Pa·s at shear rate of 1 s^{-1}, respectively. c) Examples of printed structures including 3D model, printed sample in cuvette, green body extracted and pyrolyzed: (I) gyroid, (II) shamrock, (III)

bust of Galileo Galilei, (IV) screw and gear. Scale bar is 1 mm.

2.2. Printing speed and UV irradiance

Using an optimized formulation, it was possible to print a wide range of different geometries, which were then successfully converted to ceramic parts with complex macroporous or solid structures (see **Figure 3d**). We can observe that the samples maintain the designed shapes and incur no damage both after extraction from the cuvette and pyrolysis. This suggests that the photocurable organic polymers decomposed within an appropriate temperature range for supporting the preceramic polymer during its polymer-to-ceramic conversion, enabling its thermal crosslinking without softening and associated flow, consistent with other similar blends.[46] As expected, the produced ceramic parts are constituted of a SiOC ceramic material, as revealed by XRD and FTIR analyses (see **Figure S5 and S6**). XRD analysis indicates the presence of an amorphous phase after pyrolysis at 1000°C, without the formation of crystalline phases such as SiO_2 or SiC, which is typical for the preceramic polymer precursor used in this work[47]. The FTIR spectrum of the pyrolyzed sample reveals the characteristic peaks attributed to Si-O-Si and Si-C. In addition, the raw materials and as printed samples, both before and after freeze drying, were characterized as well, and the corresponding bond-peak location is listed in **Table S1**. Additionally, following freeze drying, the reduction of the relative intensity of the peak attributed to the C=O bond within camphor correlates well with the elimination of most of the camphor after freeze-drying (**Table S2**).

The gyroid structure (**Figure 4a**) possesses a smooth surface without showing the evidence of any stair stepping effect, which would be typical for structures printed by DLP[48, 49]. The hollow cage (**Figure 4b**) is composed of trusses with a ~500 μm size,

and contains a ball that remains attached to the cage after pyrolysis. To avoid adhesion, in a further experiment a small sheet of paper was interposed between the ball and the hollow cubic cage prior to pyrolysis, and it was easily removed afterwards by blowing with compressed air due to its carbonization. **Figure S7** shows that the ball within the cage exhibits unhindered mobility after pyrolysis. It should be pointed out that, to enable the printing of a truss structure, a stronger intensity of the UV light was employed to alleviate the light loss on the path through the cuvette, leading to scratch-like lines (not caused by any staircase effect) on the surface of the ball-in-cage structure due to the scattering and fluctuations of UV light along the printing path. This could be mitigated by the further optimization of the resin transmittance through an additional reduction of H44 and an increase of camphor. The printed screw-gear structure with feature size of 50 μm suggests that this method for fabricating ceramic components at the micrometer scale could be of potential interest in the field of micromechanical systems.

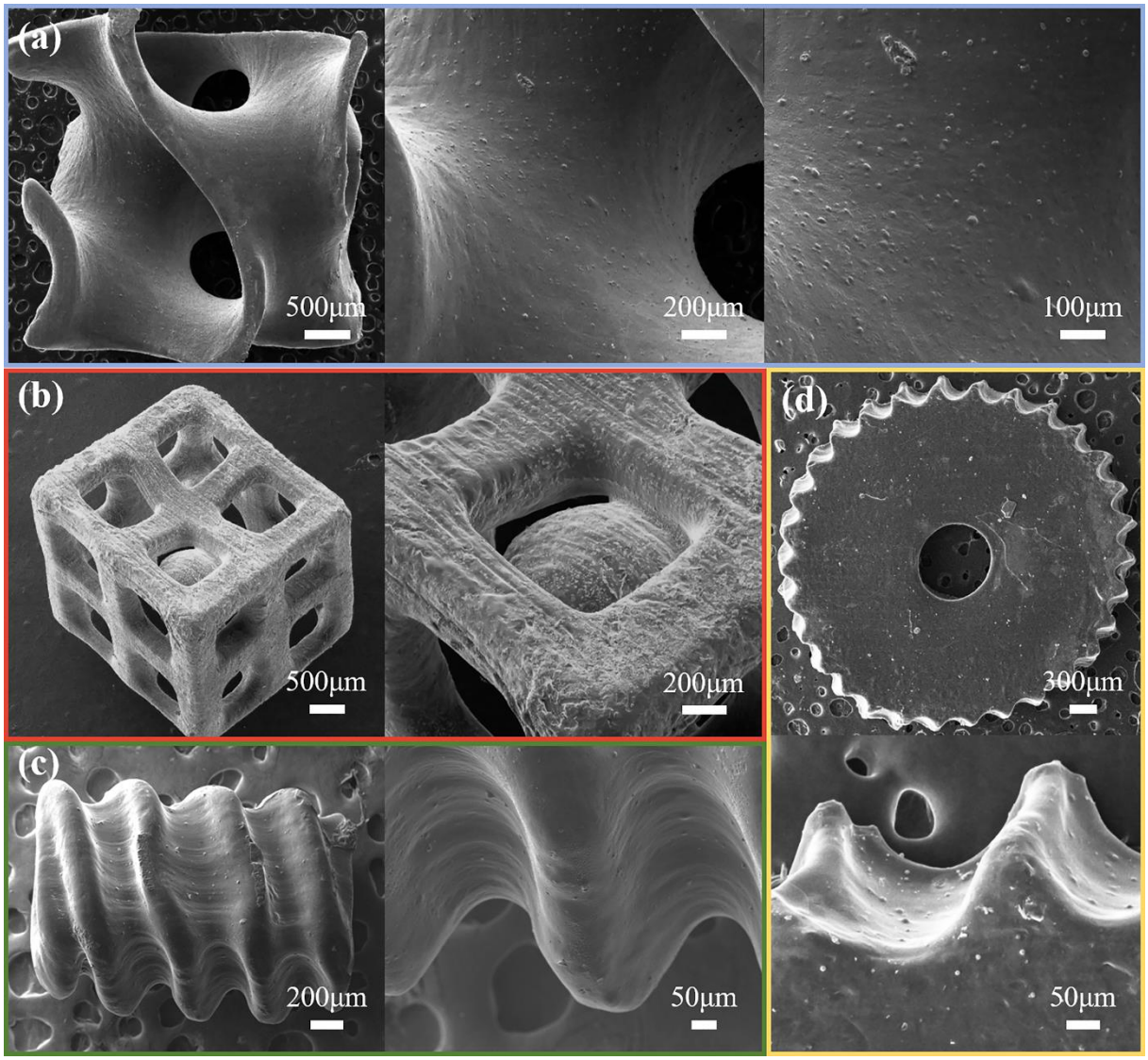

Figure 4. Microstructure of pyrolyzed samples: a) gyroid with smooth surface, b) ball-in-cage, c) screw and d) gear.

Besides the optimization of the photocurable preceramic resin, the effect of printing parameters on the printability and surface quality of the printed parts was also investigated, including the moving speed and UV irradiance. In general, three regions exist in the UV irradiance-moving speed map, as shown in **Figure S8**. When the UV irradiance exceeds a necessary threshold for a given moving speed, as determined by achieving the designed shapes and without overcuring and UV hardening on the wall (region I at lower speed), excessive UV curing near the walls of the cuvette results in

adhesion of printed parts to the cuvette. This presents difficulties in extraction and the formation of unwanted cross-linked sheets on both sides of the cuvette. Furthermore, features of printed parts tend to be incorrect in size, due to overcuring. In contrast, incomplete parts or no solidification are observed when using a smaller UV irradiance at higher moving speed (region III). This is attributed to the insufficiently activated photo-initiator failing to produce the requisite quantity of free radicals essential for initiating polymerization. Therefore, printability could only be achieved when irradiance and moving speed are within a certain range of values, depending of course on the chemistry and characteristics of the material system (region II). A bust of Galileo Galilei was printed using parameters located in region II, at a moving speed of 1 mm/min and different UV irradiance values. Comparing the different printed samples, it becomes evident that a lower irradiance level results in the absence of some of the facial features, such as a portion of the beard (**Figure 5a**). At the same time, increasing the irradiance facilitates the production of a complete printed part with clear features and a smooth surface (**Figure 5b**). Further increasing in the irradiance leads to a poorer surface quality resulting from overcuring (**Figure 5c**). In addition to a solid part, porous gyroid structures with the finest feature of 73 μm after pyrolysis (**Figure S9)** is obtained after pyrolysis, and an increase in the thickness of the sample with increasing UV irradiance is observed, indicating again that the printing parameters influence the accuracy of the printed part. Nonetheless, compared with a designed thickness of 400 μm, printed parts possess thickness varying from ~300 to ~500 μm (~150 to ~250 μm after pyrolysis considering a linear shrinkage of ~ 46%, as indicated in **Figure S9**), confirming the good geometric fidelity achievable at a given moving speed, by irradiance optimization. It's noteworthy that a low degree of cross-linking from inadequate irradiance will result in a green body that is too fragile for handling, being

prone to distortion during extraction and cleaning (**Figure S9a**), especially for parts with fine features. Although the moving speed shown here is 1 mm/min, higher speeds (3-5 mm/min, namely volumetric speed of 9-15 mm^3/min regarding cuvette size) could be possible by using a higher irradiance as well as by further optimization of the resin formulation. For the gyroid sample of 8 mm thickness in the printing direction (Fig. S7), the printing time with xolography is 8 min at a moving speed of 1 mm/min. In contrast, employing DLP technology for printing the same structure would require significantly longer durations, notably 44 min and 22 min for layer thicknesses of 25 and 50 μm, respectively. Such printing technology is time-consuming and leads to samples exhibiting poor surface quality (see in **Figure S10**). Furthermore, it is noteworthy that recent advancements in continuous feedstock feeding for xolography makes the process highly efficient[29], indicating that significant scalability opportunities exist.

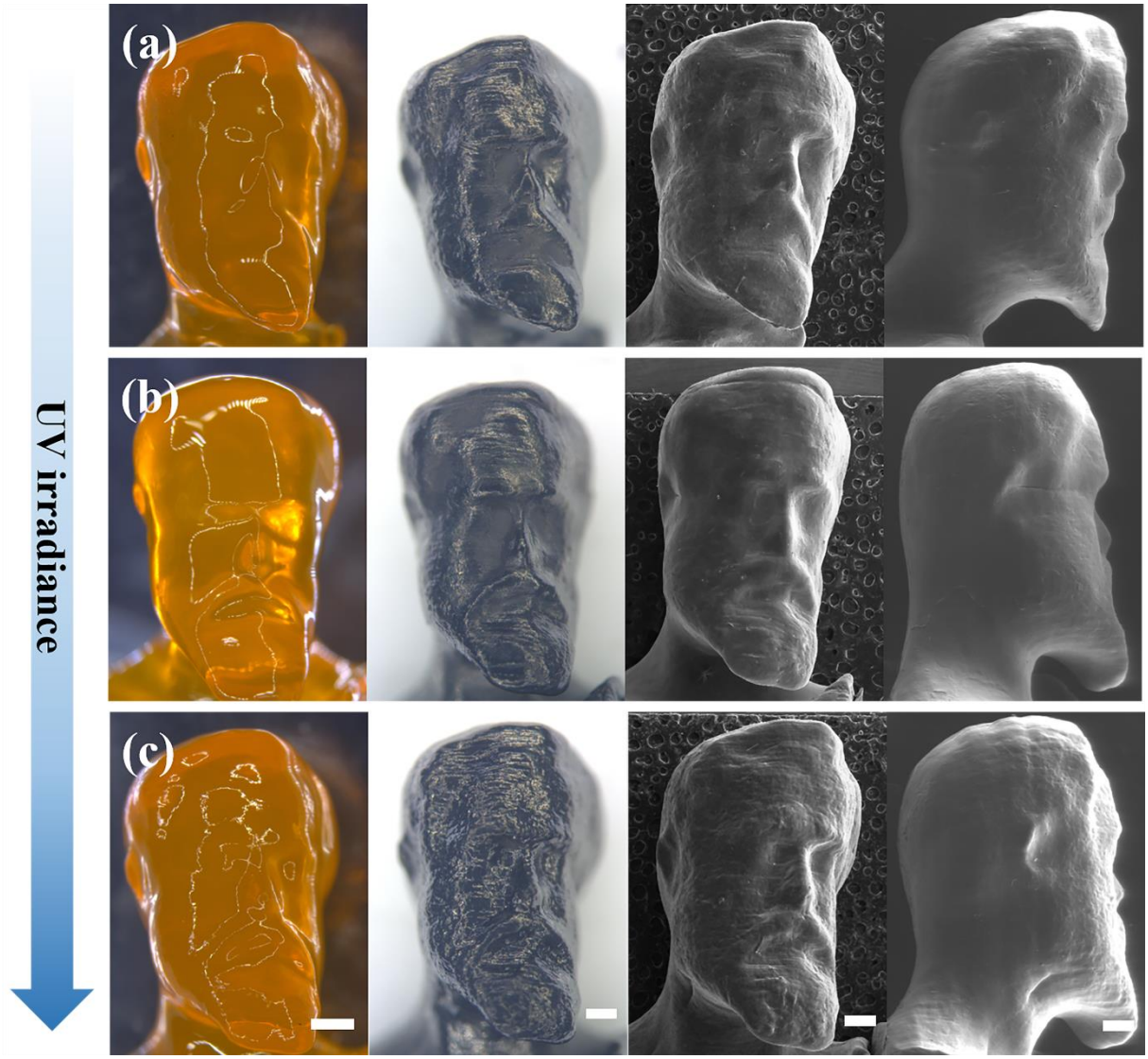

Figure 5. Bust of Galileo Galilei printed with different values for the UV irradiance, in green body (scale bar is 1 mm) and pyrolyzed forms (scale bar is 0.5 mm for digital and SEM images): a-c) 0.83, 0.86 and 0.88 mW/mm^2, respectively. Moving speed was 1 mm/min.

3. CONCLUSIONS

xolography was employed to achieve volumetric additive manufacturing of ceramic parts from a preceramic polymer. With camphor as the pore generator allowing for the release of decomposition gases during pyrolysis, complex ceramic structures with a high ratio of specific thickness over ceramic yield and without cracks were

produced, when using a suitable preceramic formulation. Smooth surfaces without stair stepping effect were obtained thanks to the continuous movement of the cuvette containing the photopolymerizable material during printing, offering relief from defects due to the formation of interfaces occurring when using traditional layer-by-layer vat photopolymerization technologies. In addition, this method extends the range of printable geometries which may be difficult to achieve without the presence of supports using other AM techniques, such as a ball-in-cage architecture. Although the minimum feature size in these experiments was ~100 μm, additional optimization of the resin formulation and light source system would enable to further improve resolution.

EXPERIMENTAL PROCEDURE

A commercially available silicone resin (SILRES® H44, Wacker-Chemie GmbH, München, Germany) was used as the ceramic precursor. Diurethane dimethacrylate (UDMA, Merck KGaA, Darmstadt, Germany) and poly (ethylene glycol) diacrylate (PEGDA) were employed as the monomers for photopolymerization, coupled with a proprietary dual-color photo-initiator (DCPI, XC471, xolo GmbH, Berlin, Germany) synthesized according to literature and provided by the company, and 1-dimethylamino-2-propanol (Merck KGaA, Darmstadt, Germany) as co-initiator.

Photocurable systems were prepared by dissolving H44 (4 or 5 g) into a mixture of 1.5 g PEGDA and 5 g UDMA, followed by adding 0.04 wt% DCPI and 9 wt% co-initiator (with respect to total weight of UDMA and PEGDA). Then, 0.17 g of fumed silica R106 (Aerosil® 106, Evonik Industries AG, Essen, Germany) for viscosity optimization and 1 g camphor (Merck KGaA, Darmstadt, Germany) as pore generator were added into the mixture, followed by mixing in a planetary mixer (ARE 250, Thinky, Japan) at 2000 rpm for 10 min. Finally, the prepared photocurable system was

transferred into a 50 ml transparent cuvette followed by 5 min centrifuging at 4000 rpm to remove residual air bubbles. The cuvette was installed on a linear stage which could move the cuvette continuously away from the projector through the optical setup using a xolographic printer (xube, xolo GmbH, Berlin, Germany). Printing parameters were optimized by varying the moving speed (from 1 to 3 mm/min) and UV irradiance (from 0.8 to 3 mW/mm^2) in different ranges of values. The feedstock used for producing samples by DLP for comparison, was identical to that employed with xolography, besides replacing 0.04 wt% DCPI with 0.1 wt% TPO (Diphenyl (2, 4, 6-trimethylbenzoyl) phosphine Oxide, TCI, Japan) and adding 0.02 wt % Sudan R (TCI, Japan) as photo-absorber. A DLP printer (Asiga Max 2, NSW, Australia) was used to fabricate the samples. For sample with layer thickness of 50 μm, UV intensity was 25 mW/cm^2 and exposure time was 1.5 s; for sample with layer thickness of 25 μm, UV intensity was 20 mW/cm^2 and exposure time was 1.5 s.

The printed samples were cleaned using isopropanol with manual agitation for 1 min and blow dried using compressed air. After removal of the uncured liquid, the samples were transferred into a freeze dryer (FreeZone2.5, Labconco, Kansas, USA) for a night, at a temperature of -52 ℃ and a pressure of 0.25 mbar. Following freeze drying, samples were then pyrolyzed at 1000°C in a tube furnace in flowing nitrogen (99.99%), according to the heating schedule reported in **Figure S11**.

The morphology of the printed structures before and after pyrolysis was characterized by optical stereomicroscopy (Stemi 2000-C, Carl Zeiss, Oberkochen, Germany) and scanning electron microscopy (FEI Quanta 200 ESEM, Eindhoven, The Netherlands). The ceramic yield was investigated by thermo-gravimetric (TG) analysis (STA409, Netzsch, Germany) from room temperature to 1000℃ with a heating rate of 5℃/min, under N_2 atmosphere. Transmittance curves were obtained using a

spectrometer (V-650 UV-VIS Spectrophotometer, Jasco, Germany). X-ray diffraction (XRD, AXS D8 Advance, Bruker,Germany) was employed to investigate the phase composition. Fourier-transform infrared spectrometry (FTIR, Is10, Nicolet, Thermo Scientific, USA) was used to characterize raw materials, as printed and pyrolyzed samples. Sample sizes before and after pyrolysis were measured with a digital caliper.

Supporting Information

Supporting Information is available online or from the author.

Acknowledgements

K.H. gratefully acknowledges the support of the China Scholarship Council (CSC) (No. 201804910741). This study was carried out within the MICS (Made in Italy – Circular and Sustainable) Extended Partnership and received funding from the European Union Next-GenerationEU (PIANO NAZIONALE DI RIPRESA E RESILIENZA (PNRR) – MISSIONE 4 COMPONENTE 2, INVESTIMENTO 1.3–D.D.1551.11–10-2022, PE00000004). This manuscript reflects only the authors' views and opinions, neither the European Union nor the European Commission can be considered responsible for them. Niklas König (xolo GmbH, Germany) is gratefully acknowledged for fruitful discussions.

Conflicts of interest

The authors declare no conflict of interest.

References

1. Chaudhary, R. P.; Parameswaran, C.; Idrees, M.; Rasaki, A. S.; Liu, C.; Chen, Z.; Colombo, P., *Progress in Materials Science* **2022**, 100969.
2. Franchin, G.; Elsayed, H.; Botti, R.; Huang, K.; Schmidt, J.; Giometti, G.; Zanini, A.; De Marzi, A.; D'Agostini, M.; Scanferla, P., *Chinese Journal of Mechanical Engineering: Additive Manufacturing Frontiers* **2022**, 100012.
3. Dadkhah, M.; Tulliani, J.-M.; Saboori, A.; Iuliano, L., *Journal of the European Ceramic Society* **2023**.
4. Lacelle, T.; Sampson, K. L.; Yazdani Sarvestani, H.; Rahimizadeh, A.; Barroeta Robles, J.; Mirkhalaf, M.; Rafiee, M.; Jakubinek, M. B.; Paquet, C.; Ashrafi, B., *APL Materials* **2023,** *11* (7).
5. Zanchetta, E.; Cattaldo, M.; Franchin, G.; Schwentenwein, M.; Homa, J.; Brusatin, G.; Colombo, P., *Adv Mater* **2016,** *28* (2), 370-376. DOI 10.1002/adma.201503470.
6. Eckel, Z. C.; Zhou, C.; Martin, J. H.; Jacobsen, A. J.; Carter, W. B.; Schaedler, T. A., *Science* **2016,** *351* (6268), 58-62.
7. Hundley, J. M.; Eckel, Z. C.; Schueller, E.; Cante, K.; Biesboer, S. M.; Yahata, B. D.; Schaedler, T. A., *Additive Manufacturing* **2017,** *18*, 95-102.
8. Xiao, J.; Jia, Y.; Liu, D.; Cheng, H., *Ceramics International* **2020,** *46* (16), 25802-25807.
9. He, C.; Ma, C.; Li, X.; Hou, F.; Yan, L.; Guo, A.; Liu, J., *Additive Manufacturing* **2021,** *46*, 102111.
10. Fu, Y.; Xu, G.; Chen, Z.; liu, C.; Wang, D.; Lao, C., *Ceramics International* **2018,** *44* (10), 11030-11038. DOI 10.1016/j.ceramint.2018.03.075.
11. Wang, X.; Schmidt, F.; Hanaor, D.; Kamm, P. H.; Li, S.; Gurlo, A., *Additive Manufacturing* **2019,** *27*, 80-90. DOI 10.1016/j.addma.2019.02.012.
12. Brodnik, N.; Schmidt, J.; Colombo, P.; Faber, K., *Additive Manufacturing* **2020,** *31*, 100957.
13. Zhang, S.; Sutejo, I. A.; Gal, C. W.; Choi, Y.-J.; Kim, H.-N.; Park, Y.-J.; Yun, H.-s., *Journal of the European Ceramic Society* **2024**.
14. Yıldız, B. K.; Yıldız, A. S.; Kul, M.; Tür, Y. K.; Işık, E.; Duran, C.; Yılmaz, H., *Ceramics International* **2024,** *50* (2), 2901-2908.
15. Pham, T. A.; Kim, D. P.; Lim, T. W.; Park, S. H.; Yang, D. Y.; Lee, K. S., *Adv Funct Mater* **2006,** *16* (9), 1235-1241.
16. Brigo, L.; Schmidt, J. E. M.; Gandin, A.; Michieli, N.; Colombo, P.; Brusatin, G., *Advanced Science* **2018**, 1800937. DOI 10.1002/advs.201800937.
17. Schmidt, J.; Brigo, L.; Gandin, A.; Schwentenwein, M.; Colombo, P.; Brusatin, G., *Additive Manufacturing* **2019,** *30*, 100913.
18. Bauer, J.; Crook, C.; Izard, A. G.; Eckel, Z. C.; Ruvalcaba, N.; Schaedler, T. A.; Valdevit, L., *Matter* **2019,** *1* (6), 1547-1556.
19. Konstantinou, G.; Kakkava, E.; Hagelüken, L.; Sasikumar, P. V. W.; Wang, J.; Makowska, M. G.; Blugan, G.; Nianias, N.; Marone, F.; Van Swygenhoven, H., *Additive Manufacturing* **2020,** *35*, 101343.
20. Sänger, J. C.; Pauw, B. R.; Riechers, B.; Zocca, A.; Rosalie, J.; Maaß, R.; Sturm, H.; Günster, J., *Adv Mater* **2023,** *35* (8), 2208653.
21. Prediger, R.; Sriyotha, N.; Schell, K. G.; Kluck, S.; Hambitzer, L.; Kotz-Helmer, F., *Advanced Science* **2024**, 2307175.
22. Astm, I., *ASTM International, West Conshohocken, PA* **2015,** *3* (4), 5.
23. Monzón, M.; Ortega, Z.; Hernández, A.; Paz, R.; Ortega, F., *Materials* **2017,** *10*

(1), 64.
24. Bennour, M.; Saidi, F.; Bouzaïene, L.; Sfaxi, L.; Maaref, H., *Journal of applied physics* **2012,** *111* (2), 024310.
25. Tumbleston, J. R.; Shirvanyants, D.; Ermoshkin, N.; Janusziewicz, R.; Johnson, A. R.; Kelly, D.; Chen, K.; Pinschmidt, R.; Rolland, J. P.; Ermoshkin, A., *Science* **2015,** *347* (6228), 1349-1352.
26. Lipkowitz, G.; Samuelsen, T.; Hsiao, K.; Lee, B.; Dulay, M. T.; Coates, I.; Lin, H.; Pan, W.; Toth, G.; Tate, L., *Sci Adv* **2022,** *8* (39), eabq3917.
27. Huang, Z.; Shao, G.; Zhou, D.; Deng, X.; Qiao, J.; Li, L., *International Journal of Extreme Manufacturing* **2023,** *5* (3), 035501.
28. Regehly, M.; Garmshausen, Y.; Reuter, M.; König, N. F.; Israel, E.; Kelly, D. P.; Chou, C.-Y.; Koch, K.; Asfari, B.; Hecht, S., *Nature* **2020,** *588* (7839), 620-624.
29. Stüwe, L.; Geiger, M.; Röllgen, F.; Heinze, T.; Reuter, M.; Wessling, M.; Hecht, S.; Linkhorst, J., *Adv Mater* **2023**, 2306716.
30. Kelly, B. E.; Bhattacharya, I.; Heidari, H.; Shusteff, M.; Spadaccini, C. M.; Taylor, H. K., *Science* **2019,** *363* (6431), 1075-1079.
31. Loterie, D.; Delrot, P.; Moser, C., *Nature communications* **2020,** *11* (1), 1-6.
32. Cook, C. C.; Fong, E. J.; Schwartz, J. J.; Porcincula, D. H.; Kaczmarek, A. C.; Oakdale, J. S.; Moran, B. D.; Champley, K. M.; Rackson, C. M.; Muralidharan, A.; McLeod, R. R.; Shusteff, M., *Adv Mater* **2020,** *32* (47), e2003376. DOI 10.1002/adma.202003376.
33. Toombs, J. T.; Luitz, M.; Cook, C. C.; Jenne, S.; Li, C. C.; Rapp, B. E.; Kotz-Helmer, F.; Taylor, H. K., *Science* **2022,** *376* (6590), 308-312.
34. Riffe, M. B.; Davidson, M. D.; Seymour, G.; Dhand, A. P.; Cooke, M. E.; Zlotnick, H. M.; McLeod, R. R.; Burdick, J. A., *Adv Mater* **2024**, e2309026. DOI 10.1002/adma.202309026.
35. Chen, T.; You, S.; Xu, L.; Cao, C.; Li, H.; Kuang, C.; Liu, X., *Additive Manufacturing* **2024,** *80*, 103968. DOI 10.1016/j.addma.2024.103968.
36. Myers, L. A.; Schwartz, J. J.; De Beer, M. P.; Walton, R. L.; Porcincula, D. H., *Journal of Polymer Science* **2024**.
37. Lian, L.; Xie, M.; Luo, Z.; Zhang, Z.; Maharjan, S.; Mu, X.; Garciamendez-Mijares, C. E.; Kuang, X.; Sahoo, J. K.; Tang, G., *Adv Mater* **2024**, 2304846.
38. Corrigan, N.; Li, X.; Zhang, J.; Boyer, C., *Advanced Materials Technologies* **2024**.
39. Kollep, M.; Konstantinou, G.; Madrid-Wolff, J.; Boniface, A.; Hagelüken, L.; Sasikumar, P. V. W.; Blugan, G.; Delrot, P.; Loterie, D.; Brugger, J.; Moser, C., *Adv Eng Mater* **2022**, 2101345. DOI 10.1002/adem.202101345.
40. Gruber, H. F., *Progress in polymer Science* **1992,** *17* (6), 953-1044.
41. Kloosterboer, J. G., Network formation by chain crosslinking photopolymerization and its applications in electronics. In *Electronic applications*, Springer: 1988; pp 1-61.
42. Allushi, A.; Kutahya, C.; Aydogan, C.; Kreutzer, J.; Yilmaz, G.; Yagci, Y., *Polymer Chemistry* **2017,** *8* (12), 1972-1977. DOI 10.1039/c7py00114b.
43. Xiong, S.; Liu, J.; Cao, J.; Li, Z.; Idrees, M.; Lin, X.; Long, Z.; Liu, Z.; Wang, P.; Liu, C., *Additive Manufacturing* **2022,** *57*, 102964.
44. Wilhelm, M.; Soltmann, C.; Koch, D.; Grathwohl, G., *Journal of the European Ceramic Society* **2005,** *25* (2-3), 271-276.
45. Stokes, G. G., *Trans. Cambridge Philos. Soc.* **1901,** *9*, 1-141.
46. Schmidt, J.; Colombo, P., *Journal of the European Ceramic Society* **2018,** *38* (1), 57-66.
47. Zhang, J.; Chen, H.; Wei, J.; Zhang, Y.; Wang, L., *International Journal of*

Applied Ceramic Technology **2023,** *20* (1), 313-320.
48. Feng, Y.; Guo, X.; Huang, K.; Elsayed, H.; Franchin, G.; Gong, H.; Colombo, P., *Journal of the European Ceramic Society* **2021**. DOI 10.1016/j.jeurceramsoc.2021.06.007.
49. He, X.; Wang, R.; Qi, S.; Cheng, J.; Ye, H.; Li, H.; Chen, S.; Jian, B.; Ge, Q., *Additive Manufacturing* **2023,** *78*, 103889.